

# Frequency-domain Green's functions for radar waves in heterogeneous 2.5D media

Karl J. Ellefsen<sup>1</sup>, Delphine Croizé<sup>2</sup>, Aldo T. Mazzella<sup>3</sup>, and Jason R. McKenna<sup>4</sup>

## ABSTRACT

Green's functions for radar waves propagating in heterogeneous 2.5D media might be calculated in the frequency domain using a hybrid method. The model is defined in the Cartesian coordinate system, and its electromagnetic properties might vary in the  $x$ - and  $z$ -directions, but not in the  $y$ -direction. Wave propagation in the  $x$ - and  $z$ -directions is simulated with the finite-difference method, and wave propagation in the  $y$ -direction is simulated with an analytic function. The absorbing boundaries on the finite-difference grid are perfectly matched layers that have been modified to make them compatible with the hybrid method. The accuracy of these numerical Green's functions is assessed by comparing them with independently calculated Green's functions. For a homogeneous model, the magnitude errors range from  $-4.16\%$  through  $0.44\%$ , and the phase errors range from  $-0.06\%$  through  $4.86\%$ . For a layered model, the magnitude errors range from  $-2.60\%$  through  $2.06\%$ , and the phase errors range from  $-0.49\%$  through  $2.73\%$ . These numerical Green's functions might be used for forward modeling and full waveform inversion.

## INTRODUCTION

A Green's function for a radar wave mathematically represents the wave generated by an infinitesimal electric dipole. Green's functions are important because they might be used for full waveform inversion (Pratt et al., 1998; Ellefsen et al., 2007) and forward modeling. Despite their utility, they have been formulated analytically for only homogeneous, layered, and waveguide models (Tai, 1971; Chew, 1990; Jin, 2002). Such models rarely are suitable representations of

typical geologic media. Indeed, typical media are very heterogeneous, so the calculation of Green's functions requires numerical methods, such as the finite-difference method or the finite-element method.

Recently, the frequency-domain, finite-difference method has been used for forward modeling and inversion of electromagnetic induction data with 3D models (Smith, 1996; Oristaglio and Spies, 1999; Champagne et al., 2001; Weiss and Newman, 2002; Hou et al., 2006). The frequencies of electromagnetic data typically are less than 100 KHz, whereas the frequencies of radar data typically are greater than 50 MHz. At these relatively high frequencies, the finite-difference grid must be dense to ensure that radar waves are simulated accurately. Such a dense 3D grid would yield enormous models, for which forward modeling and inversion of radar data would be impractical. Thus, the numerical methods developed for electromagnetic data generally are unsuitable for radar data.

To overcome this difficulty, we developed a hybrid method to calculate Green's functions for radar waves in 2.5D heterogeneous models. Such a hybrid method has not been developed previously for radar waves. The hybrid method uses the frequency-domain, finite-difference method to simulate wave propagation in two spatial dimensions and uses an analytic expression to simulate propagation in the third spatial dimension. Thus, Green's functions calculated for 2.5D models equal Green's functions calculated for equivalent 3D models. A significant advantage of this hybrid method is that the 2.5D model is much smaller than an equivalent 3D model; thus, forward modeling and inversion with the hybrid method are practical.

In this article, we present the hybrid method. A unique feature of the method is the perfectly matched layers that account for complex frequency, making them compatible with the hybrid method. We test the accuracy of Green's functions by comparing them with independently calculated Green's functions for homogeneous and layered models, and we demonstrate how this hybrid method can be used for forward modeling of crosswell radar data.

Manuscript received by the Editor 2 June 2008; revised manuscript received 24 November 2008; published online 2 April 2009.

<sup>1</sup>U. S. Geological Survey, Denver, Colorado, U.S.A. E-mail: ellefsen@usgs.gov.

<sup>2</sup>University of Oslo, Oslo, Norway. E-mail: delphine.croize@geo.uio.no.

<sup>3</sup>U. S. Environmental Protection Agency, Las Vegas, Nevada, U.S.A. E-mail: mazzella.aldo@epa.gov.

<sup>4</sup>U. S. Army Engineer Research & Development Center, Vicksburg, Mississippi, U.S.A. E-mail: Jason.R.McKenna@usace.army.mil.

## METHOD

### Mathematical model

In the model, locations are specified using a rectangular Cartesian coordinate system whose  $x$ -axis is horizontal,  $z$ -axis is vertical, and  $y$ -axis is chosen to make the coordinate system right-handed. The electromagnetic properties of the model might depend upon frequency, and the constitutive equations are linear. The electromagnetic properties might vary in the  $x$ - and  $z$ -directions, but not in the  $y$ -direction. Because the calculation of the Green's functions can account for propagation in the  $y$ -direction, the model is called 2.5D.

The transmitting antenna is an infinitesimal electric dipole that could have any orientation relative to the Cartesian coordinate system, and the receiving antenna records any of the three components of the electric field. Although the transmitting and receiving antennas could be located anywhere within the model, they usually are near the  $x$ - $z$ -plane.

### Calculating numerical Green's functions

In the frequency domain, the two Maxwell's equations that relate the electric field  $\mathbf{E}$  and magnetic field  $\mathbf{H}$  are

$$\nabla \times \mathbf{E} + Z\mathbf{H} = -\mathbf{M} \quad (1a)$$

and

$$\nabla \times \mathbf{H} - Y\mathbf{E} = \mathbf{J}, \quad (1b)$$

where  $\mathbf{M}$  is the magnetic current density in an infinitesimal magnetic dipole, and  $\mathbf{J}$  is the electric current density in an infinitesimal electric dipole (Harrington, 1961, p. 19). Variable  $Z$  equals  $-i\omega\mu$ , where  $i$  is  $\sqrt{-1}$ ,  $\omega$  is the angular frequency, and  $\mu$  is the magnetic permeability. Variable  $Z$  has dimensions of impedance per length and is called *impedivity* by Harrington (1961, p. 19). Variable  $Y$  equals  $-i(\omega\epsilon + i\sigma)$ , where  $\epsilon$  is the dielectric permittivity and  $\sigma$  is the electrical conductivity. Variable  $Y$  has dimensions of admittance per length and is called *admittivity* by Harrington (1961, p. 19). In equations 1a and 1b, the harmonic time variation is  $\exp(-i\omega t)$ , which is the complex conjugate of that used by Harrington (1961, p. 15–19).

To simulate radar waves generated by an electric dipole, the magnetic current density in equation 1a is assumed to be zero. The angular frequency is replaced by a complex angular frequency  $\omega_c$  with real part  $\omega_r$  and imaginary part  $\omega_i$ ; this complex angular frequency is needed to implement the discrete wavenumber method, which is discussed later. Then these two first-order differential equations are combined into a second-order differential equation:

$$\nabla \times \left( \frac{1}{Z} \nabla \times \mathbf{E} \right) + Y\mathbf{E} = -\mathbf{J}, \quad (2)$$

which is an inhomogeneous vector wave equation involving only the electric field. Although this equation lacks any explicit expression for the magnetic field  $\mathbf{H}$ , it completely describes the physics of a propagating radar wave (see, e.g., Stratton, 1941, p. 270).

A spatial Fourier transform in the  $y$ -direction is applied to equation 2. In the transformed equation, the components of the electric field and the electric current density are represented by  $\tilde{E}_x, \tilde{E}_y, \tilde{E}_z$  and  $\tilde{J}_x, \tilde{J}_y, \tilde{J}_z$ , respectively. These transformed components are now functions of  $k_y$ , which is the  $y$ -component of the wavenumber. The implicit assumption in this transformation is that wave propagation in

the  $y$ -direction is simulated with the analytic expression  $\exp(ik_y y)$ . The transformed equation 2 comprises three coupled differential equations:

$$k_y^2 \frac{1}{Z} \tilde{E}_x - \frac{\partial}{\partial z} \left( \frac{1}{Z} \frac{\partial \tilde{E}_x}{\partial z} \right) + Y \tilde{E}_x + ik_y \frac{1}{Z} \frac{\partial \tilde{E}_y}{\partial x} + \frac{\partial}{\partial z} \left( \frac{1}{Z} \frac{\partial \tilde{E}_z}{\partial x} \right) = -\tilde{J}_x, \quad (3a)$$

$$ik_y \frac{\partial}{\partial x} \left( \frac{1}{Z} \tilde{E}_x \right) - \frac{\partial}{\partial x} \left( \frac{1}{Z} \frac{\partial \tilde{E}_y}{\partial x} \right) - \frac{\partial}{\partial z} \left( \frac{1}{Z} \frac{\partial \tilde{E}_y}{\partial z} \right) + Y \tilde{E}_y + ik_y \frac{\partial}{\partial z} \left( \frac{1}{Z} \tilde{E}_z \right) = -\tilde{J}_y, \quad (3b)$$

and

$$\frac{\partial}{\partial x} \left( \frac{1}{Z} \frac{\partial \tilde{E}_x}{\partial z} \right) + ik_y \frac{1}{Z} \frac{\partial \tilde{E}_y}{\partial z} + k_y^2 \frac{1}{Z} \tilde{E}_z - \frac{\partial}{\partial x} \left( \frac{1}{Z} \frac{\partial \tilde{E}_z}{\partial x} \right) + Y \tilde{E}_z = -\tilde{J}_z. \quad (3c)$$

These coupled equations are solved by the finite-difference method. To this end, the  $x$ - $z$ -plane of the model is divided into many small cells, within which the electromagnetic properties are constant. The three coupled equations are approximated by three difference equations (Appendix A). Along the edges of the model, the three difference equations are modified so that simulated waves are not reflected from the edges. These absorbing boundaries are implemented as perfectly matched layers and are discussed later.

The difference equations for the entire model are combined into a system of linear equations

$$\mathbf{A}\mathbf{g} = \mathbf{j}, \quad (4)$$

where  $\mathbf{A}$  is a sparse, square, complex-valued matrix, and  $\mathbf{g}$  and  $\mathbf{j}$  are complex-valued vectors. From equations 3a–3c, matrix  $\mathbf{A}$  incorporates the impedivity, admittivity, wavenumber component  $k_y$ , and finite-difference approximations of the derivatives. Matrix  $\mathbf{A}$  is assembled from these quantities using standard procedures, which are described in Champagne et al. (2001), for example. Vector  $\mathbf{g}$  incorporates the finite-difference approximations of the three components  $\tilde{E}_x, \tilde{E}_y$ , and  $\tilde{E}_z$  at the grid points; likewise, vector  $\mathbf{j}$  incorporates the finite-difference approximations of the three components  $\tilde{J}_x, \tilde{J}_y$ , and  $\tilde{J}_z$  at the grid points. The system of linear equations 4 is solved for vector  $\mathbf{g}$ .

Because the transmitting antenna is represented by an infinitesimal electric dipole, vector  $\mathbf{j}$  is a discrete representation of a Dirac delta function in space. Consequently, vector  $\mathbf{g}$  is a numerical Green's function for the entire model at complex angular frequency  $\omega_c$  and wavenumber component  $k_y$ .

To understand how the numerical Green's function in the spatial  $y$ -domain is calculated, assume that the receiving antenna records the  $x$ -component of the electric field resulting from an electric dipole oriented in the  $z$  direction. The element of vector  $\mathbf{g}$  corresponding to this component is  $\tilde{G}_{xz}(x, k_y, z, \omega_c)$ , and this element is integrated over  $k_y$ :

$$G_{xz}(x, y, z, \omega_c) = \frac{1}{2\pi} \int_{-\infty}^{\infty} \tilde{G}_{xz}(x, k_y, z, \omega_c) e^{ik_y(y-y_t)} dk_y, \quad (5)$$

where  $y_t$  is the  $y$ -coordinate of the transmitting antenna. In practice, the integral is computed via the discrete wavenumber method (Bouchon, 2003), for which the angular frequency must be complex. The discrete wavenumber method essentially replaces the integral with a summation in which each term pertains to a different value of  $k_y$ . Hence, for each term in the summation,  $\tilde{G}_{xz}(x, k_y, z, \omega_c)$  is computed by solving the system of linear equations 4. The implementation of the discrete wavenumber method is described in Appendix B; this implementation exploits symmetry in the electric fields to halve the amount of computation. The integral in equation 5 also might be computed with Gaussian-Legendre integration (Zhou and Greenhalgh, 2006).

### Perfectly matched layers

Recall that the absorbing boundaries are implemented as perfectly matched layers. To be used with the hybrid method, these perfectly matched layers must be adapted for complex angular frequency; this adaptation is described in this section. This section omits details regarding the implementation of perfectly matched layers because this information is found elsewhere (Rappaport et al., 2000; Taflove and Hagness, 2000, p. 285–348).

Consider the boundary on the right side of the finite-difference grid, which is normal to the  $x$ -direction. For this boundary, the coordinate  $x$  is replaced by a stretched coordinate  $x'$  via the equation

$$x' = x \left[ 1 + \left( 1 + i \frac{k_{xR}}{k_{xI}} \right) a(x) \right], \quad (6)$$

where  $k_{xR}$  and  $k_{xI}$  are the real and imaginary parts of the wavenumber in the  $x$ -direction. This complex wavenumber depends upon the complex angular frequency and the electromagnetic properties of the medium. Function  $a(x)$  is nonnegative real and is described later.

To see the effect of the stretched coordinate, substitute equation 6 into an exponential that describes wave propagation in the  $x$ -direction:

$$\begin{aligned} \exp[i(k_{xR} + ik_{xI})x'] &= \exp[i(k_{xR} + ik_{xI})x] \\ &\times \exp[-(k_{xI} + k_{xR}^2/k_{xI})a(x)x]. \end{aligned} \quad (7)$$

The exponential on the left side of equation 7 is reexpressed using the two exponentials on the right side. The first describes the change in the amplitude and the phase resulting from propagation, but not stretching. The second exponential describes the decrease in the amplitude of the wave resulting from stretching. Thus, the only effect of the stretching, and hence the only effect of the perfectly matched layer, is to attenuate the wave in the  $x$ -direction.

A common choice for function  $a(x)$  is a simple polynomial (Taflove and Hagness, 2000, p. 306):

$$a(x) = a_m \left( \frac{x - x_{\text{PML}}}{T} \right)^p, \quad (8)$$

where  $x_{\text{PML}}$  is the  $x$ -coordinate at the beginning of the perfectly matched layer;  $a_m$  is the maximum value of  $a(x)$ ;  $p$  is a positive real

number, usually between 3 and 4; and  $T$  is the thickness of the perfectly matched layer. Selecting a suitable value for  $a_m$  is described later. Equation 7 shows that the behavior of  $a(x)$  affects the attenuation of the wave. When  $x = x_{\text{PML}}$  (which corresponds to the beginning of the perfectly matched layer),  $a(x)$  equals 0, and hence the additional attenuation, which results from the perfectly matched layer (equation 7), is 0. As  $x$  increases within the perfectly matched layer,  $a(x)$  increases, and hence the additional attenuation increases. When  $x = T + x_{\text{PML}}$  (which corresponds to the outside edge of the perfectly matched layer),  $a(x)$  equals its maximum value  $a_m$ , and hence the additional attenuation is maximal.

To select a suitable value for  $a_m$ , consider the reflection coefficient for the perfectly matched layer. This reflection coefficient equals the amplitude of a plane wave after it propagates through the layer, reflects from the outside edge of the layer, and then propagates through the layer again into the main part of the finite-difference grid. (This amplitude is normalized by the amplitude of the wave incident upon the perfectly matched layer.) Using equation 7, this reflection coefficient can be readily derived:

$$R = \exp \left\{ -2 \int_{x_{\text{PML}}}^{x_{\text{PML}}+T} \left[ k_{xI} + \left( k_{xI} + \frac{k_{xR}^2}{k_{xI}} \right) a(x) \right] dx \right\}. \quad (9)$$

After assigning a suitable value for  $R$  (Taflove and Hagness, 2000, p. 307) and substituting equation 8 into equation 9,  $a_m$  is derived:

$$a_m = - \frac{(p+1)(\ln R + 2Tk_{xI})}{2T \left( k_{xI} + \frac{k_{xR}^2}{k_{xI}} \right)}. \quad (10)$$

This formula is used to compute an optimal value for  $a_m$ , which is used subsequently in equation 8 and then equation 6 to compute the coordinate stretching in the perfectly matched layer.

## ACCURACY OF GREEN'S FUNCTIONS

### Homogeneous model

The accuracy of numerical Green's functions is assessed first, using a homogeneous model. For this model, the electromagnetic properties are isotropic. The relative dielectric permittivity is 9.0, the relative magnetic permeability is 1.0, and the electrical conductivity is 1.0 mS/m. The transmitting antenna is an infinitesimal electric dipole, which is oriented in the  $z$ -direction and is located at the origin of the coordinate system. The receiving antenna records the  $z$ -component of the electric field and is located at 4.0,  $-0.1$ , and 0.1 m in the  $x$ -,  $y$ -, and  $z$ -directions, respectively.

In such a homogeneous model, the electromagnetic field has two parts: a reactive, nonradiating part and a radiating part (Stratton, 1941, p. 435–437; Balanis, 1989, p. 138). The reactive part dominates the radiating part when  $kr \ll 1$ , where  $k$  is the angular wavenumber and  $r$  is the distance from the infinitesimal dipole; the volume defined by this inequality is called the near field. Conversely, the radiating part dominates the reactive part when  $kr \gg 1$ ; the volume defined by this inequality is called the far field. Here, the near and far fields are defined as the volumes for which  $kr \leq 0.1$  and  $kr \geq 10$ , respectively. Between the near and far fields is the volume defined as the intermediate field, where the reactive and radiating parts are significant. For this homogeneous model, the receiving antenna is in the near field for frequencies less than 0.40 MHz, in the inter-

mediate field for frequencies between 0.40 and 40 MHz, and in the far field for frequencies greater than 40 MHz (Figure 1a).

Numerical Green's functions are calculated between 0 and 150 MHz, at intervals of 3.333 MHz. The imaginary part of the frequency is constant at 5 MHz, which is within the range suggested by Bouchon (2003). The spacing for the finite-difference grid is  $3.33 \times 10^{-2}$  m, which is one-twentieth of the shortest wavelength. (Such a small spacing typically is used for finite-difference, time-domain simulations with second-order accuracy in space [Taflove and Hagness, 2000, p. 114–133]). Analytic Green's functions are calculated at the same complex frequencies using Schelkunoff vector potentials, which are formulated in the frequency domain (Schelkunoff, 1943, p. 126–133; Ward and Hohmann, 1987, p. 144–148).

The magnitudes of the numerical Green's functions appear similar to the magnitudes of the analytic Green's functions, although there are small differences as the frequency increases (Figure 1b). The errors are quantified via  $100\% \times (m_n - m_a)/m_a$ , where  $m_n$  and  $m_a$  are the magnitudes of the numerical and analytic Green's functions, respectively. The errors range from  $-4.16\%$  through  $0.44\%$  (Figure 1c). From 0 through about 60 MHz, a range that includes the near, intermediate, and far fields, the errors appear weakly depen-

dent on frequency. In contrast, above about 60 MHz, a range that includes only the far field, the errors become more negative as the frequency increases, reaching their maximum negative value at 150 MHz. The error in this range results from numerical dispersion, which is inherent in the finite-difference method (Taflove and Hagness, 2000, p. 109–123).

The phases of the numerical Green's functions appear similar to the phases of the analytic Green's functions, although there are small differences as the frequency increases (Figure 1d). The errors are quantified via  $100\% \times (p_n - p_a)/\pi$ , where  $p_n$  and  $p_a$  are the phases calculated from the numerical and analytic Green's functions, respectively. The errors range from  $-0.06\%$  through  $4.86\%$  (Figure 1e). From 0 through about 60 MHz, a range that includes the near-, intermediate, and far fields, the errors appear weakly dependent on frequency. In contrast, above about 60 MHz, a range that includes only the far field, the errors become more positive as the frequency increases, reaching their maximum value at 150 MHz. Thus, the trend in the errors for the phase is similar to the trend in the errors for the magnitude, except for the algebraic sign. Again, the error in this range results from numerical dispersion.

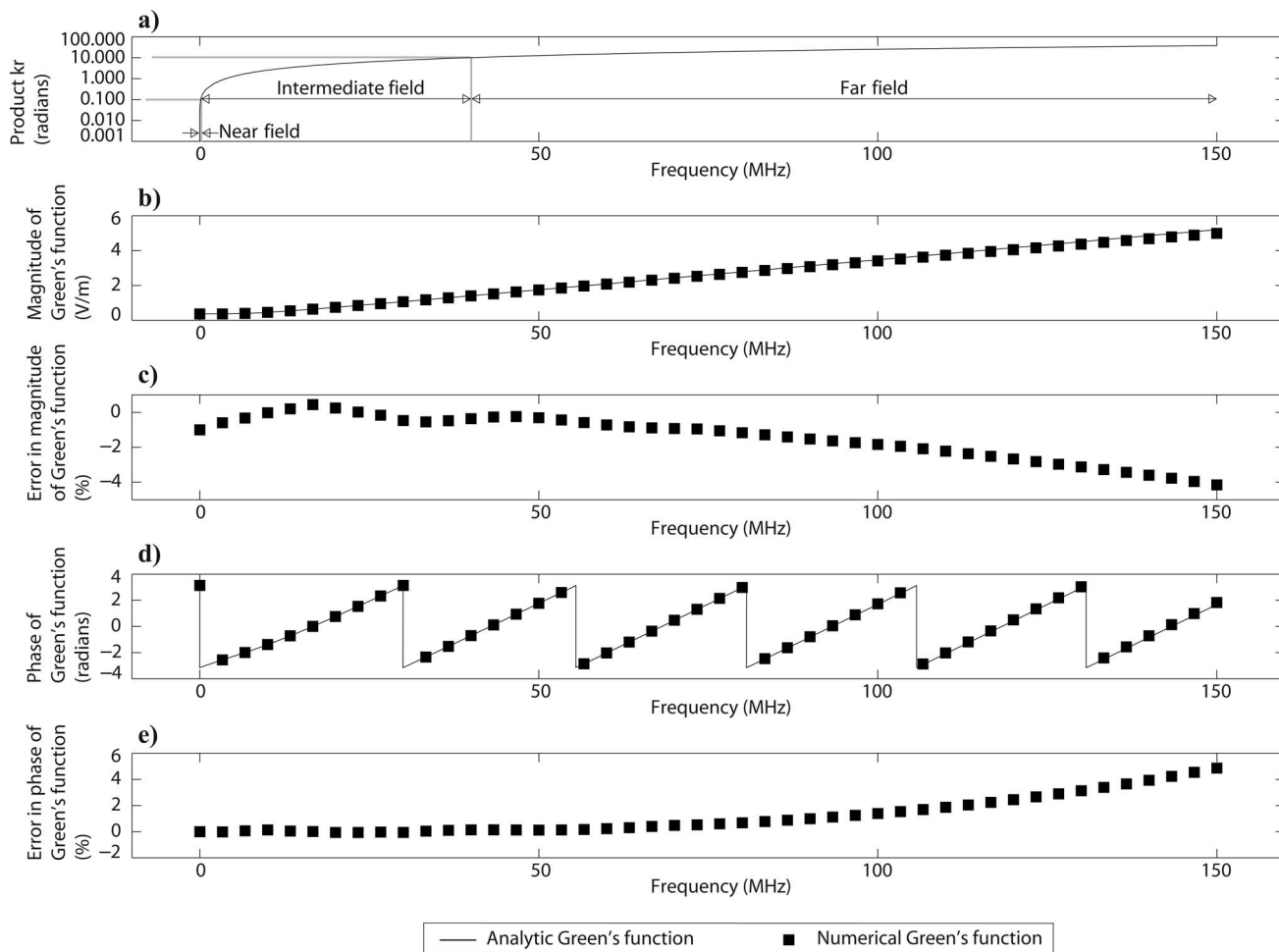


Figure 1. Accuracy of the Green's functions for the homogeneous model. (a) Frequencies associated with the near, intermediate, and far fields. (b-e) Comparisons of numerical and analytic Green's functions.

Although the results in this section demonstrate only the accuracy of  $E_z$  resulting from an electric dipole oriented in the  $z$ -direction, the accuracies of  $E_x$  and  $E_y$  resulting from the same dipole are similar. Likewise, the accuracies of the three field components resulting from a dipole oriented in the  $x$ - or  $y$ -directions are similar.

### Layered model

The accuracy of numerical Green's functions is assessed further using a model with three layers: clay, saturated sand, and clay (Figure 2). The saturated sand is 1 m thick and is between the clay layers,

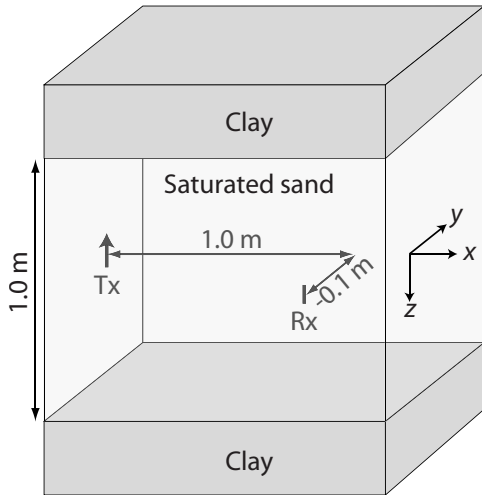


Figure 2. The layered model. Abbreviations Tx and Rx refer to the transmitting antenna and the receiving antenna, respectively.

which are half-spaces. The electromagnetic properties of the layers are isotropic. For the saturated sand, the relative dielectric permittivity is 20, the relative magnetic permeability is 1.0, and the electrical conductivity is 0.1 mS/m. For both clays, the relative dielectric permittivity is 40, the relative magnetic permeability is 1.0, and the electrical conductivity is 500 mS/m. The transmitting antenna is an infinitesimal electric dipole, which is oriented in the  $z$ -direction and is in the middle of the sand layer. The receiving antenna also is in the middle of the sand layer, but it is offset 1.0 m and  $-0.1$  m in the  $x$ - and  $y$ -directions from the transmitting antenna. The receiving antenna records the  $z$ -component of the electric field.

In this layered model, the field that is recorded at the receiving antenna might be considered as having two parts: a wave in the saturated sand that propagates directly from the transmitting to the receiving antenna, and waves that are multiply reflected from the upper and lower sand-clay interfaces. The combination of the direct and multiply reflected waves creates a guided wave — a wave whose propagation direction is guided by the layering itself (Ellefsen, 1999).

Numerical Green's functions are calculated between 0 and 300 MHz, at intervals of 12.5 MHz. The imaginary part of the frequency is constant at 12.5 MHz. The spacing for the finite-difference grid is  $1.0 \times 10^{-2}$  m, which is about one-twentieth of the shortest wavelength. Semianalytic Green's functions are calculated at the same complex frequencies using a method based on cylindrical waves (Ellefsen, 1999).

The magnitudes of the numerical Green's functions appear similar to magnitudes of the semianalytic Green's functions (Figure 3a). The errors are quantified using percentages, just as they were for the homogeneous model. The errors range from  $-2.60\%$  through  $2.06\%$  (Figure 3b). The phases of the numerical Green's functions appear similar to the phases of the analytic Green's functions (Figure

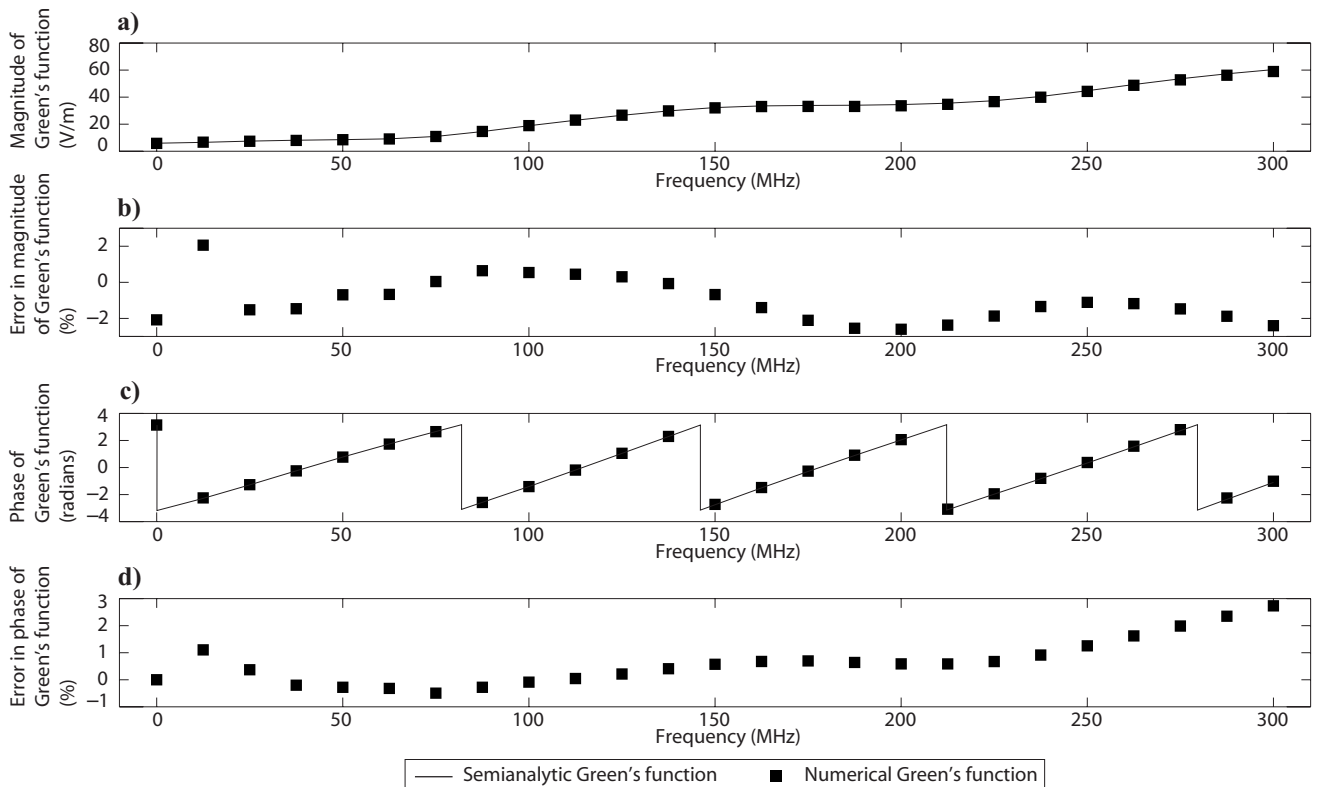


Figure 3. Accuracy of the Green's functions for the layered model. (a-d) Comparisons of numerical and semianalytic Green's functions.

3c). Again, the errors are quantified using percentages, just as they were for the homogeneous model. The errors range from  $-0.49\%$  through  $2.73\%$  (Figure 3d).

## FORWARD MODELING OF CROSSWELL RADAR DATA

Crosswell radar data were collected near Mirror Lake, which is in central New Hampshire in the United States. The bedrock consists of a pelitic schist that was first fractured and intruded by granite, then by pegmatite, and finally by diabase (Barton, 1997; Burton et al., 1999). The bedrock is completely within the saturated zone. The two boreholes pertinent to this modeling study are about 25 m apart and are deviated as much as 6.7 m from the vertical.

The crosswell radar data were collected with a radar system built by personnel at the U. S. Geological Survey. The transmitting antenna was an electric dipole with resistive loading and was 1.01 m long. The receiving antenna also was an electric dipole with resistive loading and was 1.95 m long. The housings for both antennas included metal components such as battery packs.

For the data set used in this modeling study, the transmitting antenna was stationary at a depth of 61 m in the borehole indicated on the left side of Figure 4a. The receiving antenna moved along the borehole indicated on the right side of Figure 4a; traces were recorded at 37 depths between 21 and 75 m (Figure 4b and c). This group of traces is called a common-source gather. The prominent event in the gather corresponds to a wave that propagated directly through the bedrock, from the transmitting antenna to the receiving antenna. The frequencies with high amplitudes range from about 8 through 22 MHz, and the frequency with the highest amplitude is about 17 MHz. The shape of the wavelet changes markedly with depth because the metal parts on the antenna housings affected the radar waves (Ellefsen and Wright, 2005). The traces were recorded with a sample interval of 1 ns.

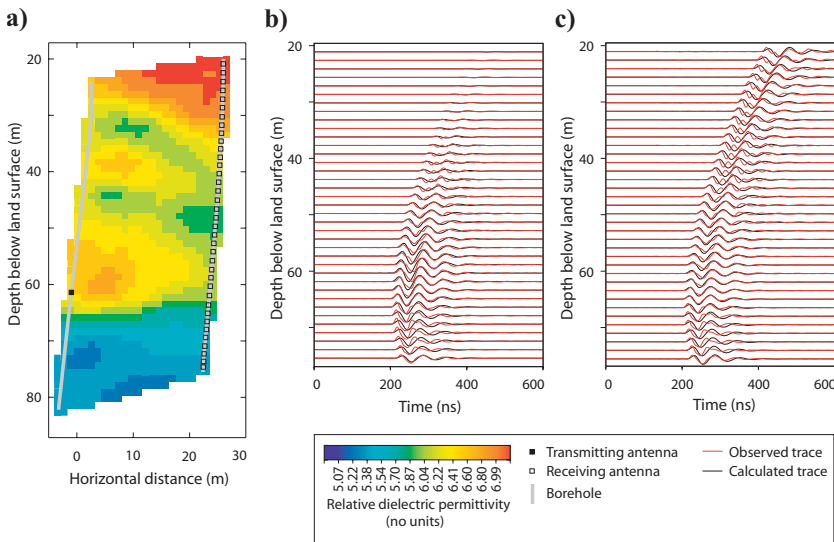


Figure 4. (a) Tomogram of the bedrock showing its relative dielectric permittivity. The locations of the antennas pertain to the common-source gather shown in (b) and (c). (b) Observed and calculated gathers, plotted with actual amplitudes. (c) Observed and calculated gathers, plotted with normalized amplitudes.

To process the traces in this gather, as well as in all other gathers, the traveltimes were picked and used to estimate the velocities with traveltime tomography, for which the algorithm is described in Ellefsen et al. (1998). The estimated velocity  $V$  was recast as relative dielectric permittivity  $\epsilon_r$  via the relation  $\epsilon_r \approx (c/V)^2$ , where  $c$  is the velocity of light in a vacuum. The estimated, relative permittivities are shown as a tomogram in Figure 4a. This tomogram pertains to only bedrock; its upper edge is near the interface between the bedrock and the overlying glacial drift. The relative permittivity generally decreases as the depth increases; this trend is attributed to the concomitant decrease in the concentration of water-filled fractures (Johnson and Dunstan, 1998, p. 33).

For the forward modeling, the relative dielectric permittivities were chosen to be those estimated with tomography (Figure 4a). All relative magnetic permeabilities were set to one, which is suitable for many rocks (e.g., Lindsley et al., 1966). All electrical conductivities were set to 1 mS/m because, in another well about 20 m away, the conductivity measured by induction logging ranged between 1 and 2 mS/m (Palliet, 1999). The transmitting antenna was represented by a vertical, infinitesimal electric dipole. Using these model parameters, numerical Green's functions were calculated for the vertical component of the electric field, which represented the signal at the receiving antenna. These Green's functions then were used to calculate traces using the method described in Appendix C. An important parameter in this method is the current density on the electric dipole that represents the transmitting antenna; this current density was chosen to be an exponentially damped sinusoid (Tsang and Rader, 1979) because it yielded a reasonable match between the calculated and the observed traces.

The match can be quantified with the relative error  $\|\mathbf{x}_c - \mathbf{x}_o\|_2 / \|\mathbf{x}_o\|_2$ , where  $\mathbf{x}_c$  is a vector containing all calculated traces from the gather,  $\mathbf{x}_o$  is a vector containing all observed traces from the gather, and  $\|\cdot\|_2$  indicates the 2-norm; this relative error could be considered as a relative root-mean-square error. If the relative error is 0, then the match between the calculated and the observed traces is perfect.

Increasing values of the relative error quantify increasing mismatch. The relative error is 0.72 for the traces in Figure 4b.

The calculated and the observed traces for the gather are shown in Figure 4b and c. Figure 4b shows that the changes in amplitude as a function of depth are the same in the calculated and the observed traces. Figure 4c shows that the traveltimes are the same in the calculated and the observed traces. Figure 4c also shows that, at depths between 45 and 65 m, the wavelets in the calculated and the observed traces generally are similar. However, at depths less than 45 m and greater than 65 m, the wavelets differ somewhat because of the previously discussed distortion of the radar wave by metal parts in the antenna housings.

## DISCUSSION

### Comparison with related methods

The hybrid method uses the finite-difference, frequency-domain method to simulate wave propagation in two spatial dimensions and uses the analytic expression  $\exp(ik_y y)$  to simulate

wave propagation in the third dimension. This mathematical methodology has been used previously in at least two other applications: [Allers et al. \(1994\)](#) developed a method to calculate electrical potential in heterogeneous 2.5D media (using very low frequencies), and [Song and Williamson \(1995\)](#) developed a method to simulate acoustic waves in heterogeneous 2.5D media. In both cases, the field equations and boundary conditions are completely different from those for radar waves, so the implementations are completely different.

### Implementation and usage

The integration in equation 5 might be considered as occurring in a complex plane representing a complex  $k_y$ . One coordinate axis in the plane represents the real part of  $k_y$ , and the other axis represents the imaginary part of  $k_y$ . The integration itself occurs along the axis for the real part of  $k_y$ . Contributions to the integral are made by poles and singularities within the complex plane, which are offset from the axis for the real part of  $k_y$  because of the imaginary part of the frequency. If the imaginary part is too small, the offset is small. Then the poles and singularities complicate the integrand, making the numerical integration inaccurate. In our experience, the inaccuracies are greatest at low frequencies (e.g., typically less than about 5 MHz). [Bouchon \(2003\)](#) suggests a suitable range of the imaginary part of the frequency; in our experience, values from this range avoid the aforementioned problem.

In practice, Green's functions usually are calculated for many different locations of the transmitting antenna. Consequently, the system of linear equations 4 must be solved for many different vectors  $\mathbf{j}$ , each of which represent a transmitting antenna. Because matrix  $\mathbf{A}$  is the same for all of these solutions, an efficient procedure to calculate these solutions is to factor matrix  $\mathbf{A}$  using LU decomposition ([Strang, 1988](#), p. 31–39). Then, the factored matrix and each  $\mathbf{j}$  are used to rapidly solve for vector  $\mathbf{g}$ . The computer resources that are needed for every solution are relatively small compared with the resources that are needed for the initial factorization.

If dielectric permittivity, magnetic permeability, or electrical conductivity depends upon frequency, new values for these properties can be calculated for each frequency. These new values are used to calculate admittivity and impedivity, which are used in the system of linear equations 4.

To simulate electromagnetic waves generated by a magnetic dipole, the electric current density in equation 1b is assumed to be zero. Then the two first-order differential equations 1a and 1b are combined into one second-order differential equation:

$$\nabla \times \left( \frac{1}{Y} \nabla \times \mathbf{H} \right) + Z\mathbf{H} = -\mathbf{J}_M, \quad (11)$$

which is an inhomogeneous vector wave equation involving only the magnetic field. The mathematical form of this equation is identical to that of equation 2, meaning the equations are duals of each other ([Harrington, 1961](#), p. 98). Because of the identical forms, the procedures used to solve equation 2 also might be used to solve equation 11. Moreover, the computer code used to solve equation 2 also might be used to solve equation 11; only the variables must be interchanged systematically.

### Future research

The partial differential equations 3a-c were implemented as finite-difference equations (6a-c in Appendix A) that have second-order

accuracy in space. With these difference equations, about twenty grid points per wavelength are needed to accurately simulate electromagnetic waves ([Taflove and Hagness, 2000](#), p. 114–133). Such a large number of grid points makes the size of matrix  $\mathbf{A}$  (equation 4) large and thereby increases the time and computer resources needed to calculate Green's functions.

Future research should focus on reducing of the size of matrix  $\mathbf{A}$ . One idea is to implement the finite-difference equations using fourth-order accuracy in space because such finite difference equations require significantly fewer grid points to accurately simulate electromagnetic waves ([Taflove and Hagness, 2000](#), p. 143–149). Another idea is to implement the finite-difference equations using convolutional differentiators ([Zhou et al., 1993](#)). For both ideas, the size of matrix  $\mathbf{A}$  (equation 4) will be smaller, but the number of off-diagonal elements in matrix  $\mathbf{A}$  will be larger. The research will determine which idea, if any, yields the greatest decrease in time and computer resources.

## CONCLUSIONS

We have developed a new method to calculate Green's functions for radar waves propagating in heterogeneous 2.5D media. The method is a hybrid: it uses the frequency-domain, finite-difference method to simulate waves in two dimensions and uses an analytic expression to simulate waves in the third dimension. An important advantage of this hybrid method is that it can account for complex geology that is encountered during many radar surveys, without resorting to 3D models that require significant computer resources. We adapted perfectly matched layers to account for complex angular frequency, making them compatible with this hybrid method; these perfectly matched layers are important because they generate significantly smaller reflections than other types of absorbing boundaries. The Green's functions calculated with the hybrid method are accurate, which was established with tests using a homogeneous model and a layered model.

An important application of this hybrid method is forward modeling of radar data; this application was demonstrated for crosswell radar data. An even more important application of this hybrid method is frequency-domain waveform inversion, for which Green's functions are needed to calculate updates to the model.

## ACKNOWLEDGMENTS AND DISCLAIMERS

The U. S. Environmental Protection Agency (USEPA), through its Office of Research and Development, partially funded and collaborated in the research described here under Interagency Agreement DW-14-93964101-1 to the U. S. Geological Survey. Although this work was reviewed by the USEPA and approved for publication, it may not reflect agency policy. Additional funding was provided by the Mineral Resources Program of the U. S. Geological Survey and by the U. S. Army Engineer Research & Development Center. The Director, Geotechnical & Structures Laboratory, U. S. Army Engineer Research & Development Center, granted permission to publish.

David Wright and Jared Abraham collected the crosswell radar data. David Fitterman, Jeffery Phillips, Viki Bankey, and several anonymous reviewers suggested changes that greatly improved this article.

Any use of trade, product, or firm names is for descriptive purposes only and does not imply endorsement by the United States government.

## APPENDIX A

### FINITE-DIFFERENCE EQUATIONS

In Appendix A, the finite-difference equations corresponding to equation 3a–3c are presented.

The  $x$ - $z$ -plane is divided into rectangular cells; within each cell, the admittivity  $Y$  and the impedivity  $Z$  are constant (Figure A-1). All cells have the same width  $\Delta x$  and the same height  $\Delta z$ ; usually  $\Delta x$  equals  $\Delta z$ . A cell, its admittivity, and its impedivity are referenced via two indices: index  $i$  pertains to the  $x$ -direction, and index  $j$  pertains to the  $z$ -direction.

The three components of the electric field within a cell are constant and are represented by  $\tilde{e}_x$ ,  $\tilde{e}_y$ , and  $\tilde{e}_z$ . Likewise, the three components of the current density within a cell are constant and are represented by  $\tilde{j}_x$ ,  $\tilde{j}_y$ , and  $\tilde{j}_z$ . The locations of these components are shown in Figure A-1. Components  $\tilde{e}_x$  and  $\tilde{j}_x$  are collocated,  $\tilde{e}_y$  and  $\tilde{j}_y$  are collocated, and  $\tilde{e}_z$  and  $\tilde{j}_z$  are collocated.

The finite-difference equations are easier to write using the following five quantities:

$$A = \frac{1}{2} \left( \frac{1}{Z_{i,j}} + \frac{1}{Z_{i,j+1}} \right), \quad (\text{A-1})$$

$$B = \frac{1}{2} \left( \frac{1}{Z_{i,j-1}} + \frac{1}{Z_{i,j}} \right), \quad (\text{A-2})$$

$$C = \frac{1}{2} \left( \frac{1}{Z_{i+1,j}} + \frac{1}{Z_{i+1,j+1}} \right), \quad (\text{A-3})$$

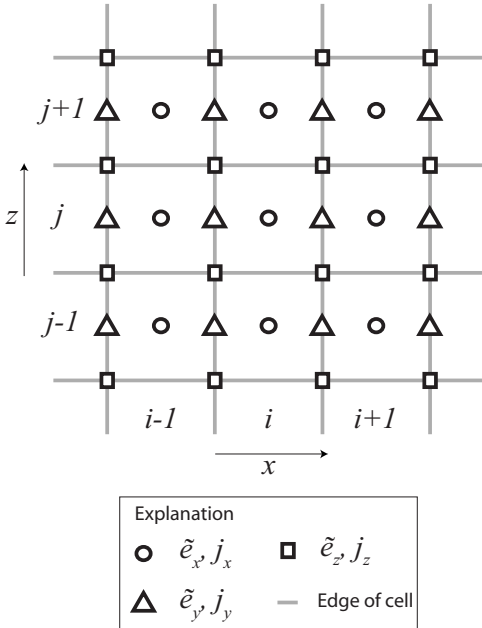


Figure A-1. Cells in the finite-difference grid. Each cell is referenced with indices  $i$  and  $j$ . Associated with each cell are three components of the electric field and three components of the current density.

$$D = \frac{1}{4} \left( \frac{1}{Z_{i+1,j+1}} + \frac{1}{Z_{i+1,j}} + \frac{1}{Z_{i,j+1}} + \frac{1}{Z_{i,j}} \right), \quad (\text{A-4})$$

$$F = \frac{1}{4} \left( \frac{1}{Z_{i+1,j}} + \frac{1}{Z_{i+1,j-1}} + \frac{1}{Z_{i,j}} + \frac{1}{Z_{i,j-1}} \right), \quad (\text{A-5})$$

The spatial derivatives in equations 3a-c are approximated with centered finite-differences. With this approximation and the quantities defined in equations A-1 through A-5, the difference equation corresponding to equation 3a is

$$\begin{aligned} & B \frac{1}{\Delta x \Delta z} \tilde{e}_z|_{i-1,j-1} - ik_y \frac{1}{Z_{i,j} \Delta x} \tilde{e}_y|_{i-1,j} - A \frac{1}{\Delta x \Delta z} \tilde{e}_z|_{i-1,j} \\ & - B \frac{1}{\Delta z^2} \tilde{e}_x|_{i,j-1} - B \frac{1}{\Delta x \Delta z} \tilde{e}_z|_{i,j-1} + \left[ Y_{i,j} + (B \right. \\ & \left. + A) \frac{1}{\Delta z^2} + k_y^2 \frac{1}{Z_{i,j}} \right] \tilde{e}_x|_{i,j} + ik_y \frac{1}{Z_{i,j} \Delta x} \tilde{e}_y|_{i,j} \\ & + A \frac{1}{\Delta x \Delta z} \tilde{e}_z|_{i,j} - A \frac{1}{\Delta z^2} \tilde{e}_x|_{i,j+1} = -\tilde{j}_x|_{i,j}. \end{aligned} \quad (\text{A-6a})$$

The difference equation corresponding to equation 3b is

$$\begin{aligned} & -\frac{1}{Z_{i,j} \Delta x^2} \tilde{e}_y|_{i-1,j} - F \frac{1}{\Delta z^2} \tilde{e}_y|_{i,j-1} - ik_y F \frac{1}{\Delta z} \tilde{e}_z|_{i,j-1} \\ & - ik_y \frac{1}{Z_{i,j} \Delta x} \tilde{e}_x|_{i,j} + \left[ \frac{1}{2} (Y_{i+1,j} + Y_{i,j}) + (D \right. \\ & \left. + F) \frac{1}{\Delta z^2} + \left( \frac{1}{Z_{i,j}} + \frac{1}{Z_{i+1,j}} \right) \frac{1}{\Delta x^2} \right] \tilde{e}_y|_{i,j} \\ & + ik_y D \frac{1}{\Delta z} \tilde{e}_z|_{i,j} - D \frac{1}{\Delta z^2} \tilde{e}_y|_{i,j+1} + ik_y \frac{1}{Z_{i+1,j} \Delta x} \tilde{e}_x|_{i+1,j} \\ & - \frac{1}{Z_{i+1,j} \Delta x^2} \tilde{e}_y|_{i+1,j} = -\tilde{j}_y|_{i,j}. \end{aligned} \quad (\text{A-6b})$$

The difference equation corresponding to equation 3c is

$$\begin{aligned} & -A \frac{1}{\Delta x^2} \tilde{e}_z|_{i-1,j} + A \frac{1}{\Delta x \Delta z} \tilde{e}_x|_{i,j} - ik_y D \frac{1}{\Delta z} \tilde{e}_y|_{i,j} \\ & + \left[ \frac{1}{4} (Y_{i+1,j+1} + Y_{i+1,j} + Y_{i,j+1} + Y_{i,j}) + k_y^2 D \right. \\ & \left. + (A + C) \frac{1}{\Delta x^2} \right] \tilde{e}_z|_{i,j} - A \frac{1}{\Delta x \Delta z} \tilde{e}_x|_{i,j+1} \\ & + ik_y D \frac{1}{\Delta z} \tilde{e}_y|_{i,j+1} - C \frac{1}{\Delta x \Delta z} \tilde{e}_x|_{i+1,j} - C \frac{1}{\Delta x^2} \tilde{e}_z|_{i+1,j} \\ & + C \frac{1}{\Delta x \Delta z} \tilde{e}_x|_{i+1,j+1} = -\tilde{j}_z|_{i,j}. \end{aligned} \quad (\text{A-6c})$$

## APPENDIX B

## IMPLEMENTATION OF THE DISCRETE WAVENUMBER METHOD

This appendix describes how the discrete wavenumber method is implemented to solve the integral in equation 5. This implementation exploits the symmetry in the electric fields to halve the amount of computation.

A simplified form of equation 5 is

$$G(y) = \frac{1}{2\pi} \int_{-\infty}^{\infty} \tilde{G}(k_y) e^{ik_y y} dk_y, \quad (\text{B-1})$$

where  $G(y)$  represents any component of the Green's function, and  $\tilde{G}(k_y)$  represents its spatial Fourier transform. Using the discrete wavenumber method, this integral is replaced by a summation:

$$G(y) \cong \frac{1}{L} \sum_{n=-N}^N \tilde{G}(k_n) e^{ik_n y}. \quad (\text{B-2})$$

Variable  $L$  is a distance, and its reciprocal is the integration interval. Variable  $n$  is an integer index, and variable  $N$  is the largest value of this index. Variable  $k_n$  is the  $y$ -component of the wavenumber and equals  $2\pi n/L$ . Criteria for selecting suitable values for  $L$  and for the imaginary part of the complex angular frequency are found in Bouchon (2003).

Because the model is symmetrical with respect to the  $x$ - $z$  plane, the kernel  $\tilde{G}(k_n)$  also is symmetrical. The symmetry depends upon the orientations of the transmitting antenna and the component of the electric field (Table B-1). Either the symmetry is even, meaning that  $\tilde{G}(k_n) = \tilde{G}(-k_n)$ , or the symmetry is odd, meaning that  $\tilde{G}(k_n) = -\tilde{G}(-k_n)$ . When the symmetry is even, the summation in equation B-2 reduces to

$$G(y) \cong \frac{1}{L} \left[ \tilde{G}(0) + 2 \sum_{n=1}^N \tilde{G}(k_n) \cos(k_n y) \right]. \quad (\text{B-3})$$

When the symmetry is odd, the summation reduces to

$$G(y) \cong \frac{1}{L} \left[ 2i \sum_{n=1}^N \tilde{G}(k_n) \sin(k_n y) \right]. \quad (\text{B-4})$$

This formula lacks the term  $\tilde{G}(0)$ , because it is zero. By this accounting for symmetry, the amount of computation is halved.

The summations in equations B-3 and B-4 are continued until two criteria are satisfied:

**Table B-1. Symmetry of the kernel  $\tilde{G}(k_n)$  in equation B-2.**

Orientation of the transmitting antenna	Component of the electric field E		
	$x$	$y$	$z$
$x$	even	odd	even
$y$	odd	even	odd
$z$	even	odd	even

$$k_n \geq \omega_R s_m \quad (\text{B-5})$$

and

$$\frac{|\tilde{G}(k_n)|}{|G(y)|} \leq \gamma. \quad (\text{B-6})$$

Variable  $s_m$  is the maximum slowness of the medium (or another suitably large slowness), and  $\gamma$  is a small value, usually between 0.005 and 0.010. The second criterion (equation B-6) is especially important at low frequencies, at which evanescent waves contribute significantly to the electric field.

## APPENDIX C

## CALCULATION OF RADAR TRACES

To calculate radar traces, assume that the receiving antenna records the  $x$ -component of the electric field resulting from an electric dipole oriented in the  $z$ -direction. The temporal variation of the current density on the transmitting antenna is  $s(t)$ , and its complex Fourier transform is  $S(\omega_c)$ . The product of  $S(\omega_c)$  and the numerical Green's function from equation 5 is transformed from the complex frequency domain to the time domain via

$$E_x(x, y, z, t) = \frac{e^{\omega t}}{2\pi} \int_{-\infty}^{\infty} d\omega_R e^{-i\omega_R t} S(\omega_c) G_{xz}(x, y, z, \omega_c), \quad (\text{C-1})$$

where  $E_x(x, y, z, t)$  is the component recorded by the receiving antenna. The integration is performed with a fast Fourier transform, and the subsequent multiplication by  $\exp(\omega t)$  removes the effect of the imaginary part of the complex angular frequency. Complex Fourier transforms such as equation C-1 are affected by nonuniqueness if the region of convergence of the transform is not specified (Lathi, 1965, p. 167–168); in this case, the region of convergence is  $t \geq 0$ , which means that both  $s(t)$  and  $E_x(x, y, z, t)$  are 0 for  $t < 0$ .

## REFERENCES

- Allers, A., A. Sezginer, and V. L. Druskin, 1994, Solution of 2.5-dimensional problems using the Lanczos decomposition: *Radio Science*, **29**, 955–963.
- Balanis, C. A., 1989, *Advanced engineering electromagnetics*: John Wiley & Sons, Inc.
- Barton, C. C., 1997, Bedrock geologic map of Hubbard Brook Experimental Forest and maps of fractures and geology in roadcuts along Interstate, 93, Grafton County, New Hampshire: U. S. Geological Survey Miscellaneous Investigations Series Map I-2562, scale 1:12,000, 2 sheets.
- Bouchon, M., 2003, A review of the discrete wavenumber method: *Pure and Applied Geophysics*, **160**, 445–465.
- Burton, W. C., T. R. Armstrong, and G. J. Walsh, 1999, Bedrock geologic framework of the Mirror Lake research site, New Hampshire, in D. W. Morganwalp and H. T. Buxton, eds., U. S. Geological Survey Toxic Substances Hydrology Program — Proceedings of the Technical Meeting: U. S. Geological Survey Water-Resources Investigations Report 99-4018C, **3**, 705–713.
- Champagne, N. J., J. G. Berryman, and H. M. Buettner, 2001, FDFD: A 3D finite-difference frequency-domain code for electromagnetic induction tomography: *Journal of Computational Physics*, **170**, 830–848.
- Chew, W. C., 1990, *Waves and fields in inhomogeneous media*: Van Nostrand Reinhold Co.
- Ellefsen, K. J., 1999, Effects of layered sediments on the guided wave in crosswell radar data: *Geophysics*, **64**, 1698–1707.
- Ellefsen, K. J., J. E. Kibler, P. A. Hsieh, and A. M. Shapiro, 1998, Crosswell seismic tomography at the USGS fractured rock research site — Data col-

- lection, data processing and tomograms: U. S. Geological Survey Open-File Report 98-510.
- Ellefsen, K. J., A. T. Mazzella, C. W. Moulton, and J. E. Lucius, 2007, An algorithm for waveform inversion of crosswell radar data: Proceedings of the Annual Symposium on the Application of Geophysics to Engineering and Environmental Problems, Environmental and Engineering Geophysical Society, unpaginated CD-ROM.
- Ellefsen, K. J., and D. L. Wright, 2005, Radiation pattern of a borehole radar antenna: *Geophysics*, **70**, no. 1, K1–K11.
- Harrington, R. F., 1961, *Time-harmonic electromagnetic fields*: McGraw-Hill.
- Hou, J., R. K. Mallan, and C. Torres-Verdin, 2006, Finite-difference simulation of borehole EM measurements in 3D anisotropic media using coupled scalar-vector potentials: *Geophysics*, **71**, no. 5, G225–G233.
- Jin, J., 2002, *The finite element method in electromagnetics*: John Wiley & Sons.
- Johnson, C. D., and A. H. Dunstan, 1998, Lithology and fracture characterization from drilling investigations in the Mirror Lake area, Grafton County, New Hampshire: U. S. Geological Survey Water-Resources Investigations Report 98-4183.
- Lathi, B. P., 1965, *Signals, systems, and communication*: John Wiley & Sons.
- Lindsley, D. H., G. E. Andreassen, and J. R. Balsley, 1966, Magnetic properties of rocks and minerals, in S. P. Clark Jr., ed., *Handbook of physical constants*, rev. ed.: Geological Society of America Memoir 97, section 25, 543–552.
- Oristaglio, M. L., and B. R. Spies, eds., 1999, *Three-dimensional electromagnetics*: SEG.
- Palliet, F. L., 1999, Geophysical reconnaissance in bedrock boreholes — Finding and characterizing the hydraulically active fractures, in D. W. Morganwalp and H. T. Buxton, eds., U. S. Geological Survey Toxic Substances Hydrology Program, Proceedings of the Technical Meeting: U. S. Geological Survey Water-Resources Investigations Report 99-4018C, v. 3, 725–733.
- Pratt, R. G., C. Shin, and G. J. Hicks, 1998, Gauss-Newton and full Newton methods in frequency-space waveform inversion: *Geophysical Journal International*, **133**, 341–362.
- Rappaport, C. M., M. Kilmer, and E. Miller, 2000, Accuracy considerations in using the PML ABC with FDFD Helmholtz equation computation: *International Journal of Numerical Modeling*, **13**, 471–482.
- Schelkunoff, S. A., 1943, *Electromagnetic waves*: D. Van Nostrand Co.
- Smith, J. T., 1996, Conservative modeling of 3D electromagnetic fields: Part II — Biconjugate gradient solution and an accelerator: *Geophysics*, **61**, 1319–1324.
- Song, Z., and P. R. Williamson, 1995, Frequency-domain acoustic-wave modeling and inversion of crosshole data: Part I — 2.5D modeling method: *Geophysics*, **60**, 784–795.
- Strang, G., 1988, *Linear algebra and its applications*: Harcourt Brace Jovanovich College Publishers.
- Stratton, J. A., 1941, *Electromagnetic theory*: McGraw-Hill.
- Taflove, A., and S. C. Hagness, 2000, *Computational electrodynamics — The finite-difference time-domain method*: Artech House.
- Tai, C. T., 1971, *Dyadic Green's functions in electromagnetic theory*: International Textbook Co.
- Tsang, L., and D. Rader, 1979, Numerical evaluation of the transient acoustic waveform due to a point source in a fluid-filled borehole: *Geophysics*, **44**, 1706–1720.
- Ward, S. H., and G. W. Hohmann, 1987, *Electromagnetic theory for geophysical applications*, in M. N. Nabighian, ed., *Electromagnetic methods in applied geophysics*: SEG, 131–311.
- Weiss, C. J., and G. A. Newman, 2002, Electromagnetic induction in a fully 3D anisotropic earth: *Geophysics*, **67**, 1104–1114.
- Zhou, B., and S. Greenhalgh, 2006, An adaptive wavenumber sampling strategy for 2.5D seismic-wave modeling in the frequency domain: *Pure and Applied Geophysics*, **163**, 1399–1416.
- Zhou, B., S. A. Greenhalgh, and J. Zhe, 1993, Numerical seismogram computations for inhomogeneous media using a short, variable length convolutional differentiator: *Geophysical Prospecting*, **41**, 751–766.